ARTICLE TYPE

Large-scale Highly Ordered Sb Nanorod Arrays Anode with High Capacity and Rate Capability for Sodium-Ion Batteries

Liying Liang, Yang Xu, Chengliang Wang, Liaoyong Wen, Yaoguo Fang, Yan Mi, Min Zhou, Huaping Zhao, and Yong Lei*

Na-ion batteries are a potential substitute to Li-ion batteries for energy storage devices. However, the poor electrochemical performance, especially capacity and rate capability are the major bottlenecks to future development. Here we propose a performance-oriented electrode structure, which is 1D
10 nanostructure arrays with large-scale high ordering, well vertical alignment, and large interval spacing. Benefiting from these structure merits, a great enhancement on electrochemical performance could be achieved. To Sb as an example, we firstly report large-scale highly ordered Sb nanorod arrays with uniform large interval spacing (190 nm). In return for this electrode design, high ion accessibility, fast electron transport, and strong electrode integrity are presented here. Used as additive- and binder-free
15 anode for Na-ion batteries, Sb nanorod arrays showed a high capacity of 620 mAh g^{-1} at the 100th cycle with a retention of 84% up to 250 cycles at 0.2 A g^{-1}, and superior rate capability for delivering reversible capacities of 579.7 and 557.7 mAh g^{-1} at 10 and 20 A g^{-1}, respectively. A full cell coupled by P2-Na$_{2/3}$Ni$_{1/3}$Mn$_{2/3}$O$_2$ cathode and Sb nanorod arrays anode was also conducted, which showed a good cycle performance up to 250 cycles, high rate capability up to 20 A g^{-1}, and large energy density up to 130 Wh
20 kg^{-1}. These excellent electrochemical performances shall pave a way to develop more applications of Sb nanorod arrays in energy storage devices.

1. Introduction

Sodium-ion batteries (SIBs) have regained increasing research interests as a potential substitute to Li-ion batteries, in particular
25 for large-scale energy storage systems, due to their low cost, abundant natural resources, and relatively low redox potential.[1,2] Since Na ions are about 55% larger in radius than Li ions, a steric limitation in many host structures is inevitably obtained, leading to slow insertion and extraction of Na ions, large volume changes,
30 and unstable solid electrolyte interphase (SEI). Therefore, it is a major challenge to find appropriate Na storage electrode materials or structures for high performance SIBs.[3,4]

It is widely accepted that vertically aligned 1D nanostructure arrays is an efficient electrode configuration to enhance the
35 electrochemical performance of batteries.[5-8] However, the majority of reported arrays still existed some defects on their electrode structure design, which seriously weakened the electrochemical performance. Those arrays showed more or less agglomerated morphology instead of perfect vertical alignment,
40 in which the joint parts tended to break since the stress existed among these nanostructures upon cycling, resulting in the pulverization and collapse of the electrode. Meanwhile, limited interval spacing in attached arrays lowered the ion transport rate to the deep portions of the electrode, which is not conducive to
45 high rate capability. Although using nanostructure arrays as

electrodes omits the complex process of mixing carbon black and binder, the conductivity of most of arrays is not good enough to support the electrode to finish fast charge and discharge processes and still keep high capacity and long cycle life.[9-12]

50 Recently, we reported a nanoimprinted AAO templating technique to fabricate 1D nanostructure arrays with perfect long-range regularity, fine size controllability, and very large area (up to cm^2).[13-15] Especially, using this technique, perfectly vertically aligned 1D nanostructure arrays with large interval spacing (*e.g.*
55 about 200 and 400 nm interval spacing by using different template cell size of 400 and 800 nm, and the definition of interval spacing and cell size is shown in Scheme 1X) are achievable. However, so far, there is very few report on the end of SIBs using such 1D nanostructure arrays electrode.[16] We
60 believe that, using these 1D nanostructure arrays with large-scale high ordering, well vertical alignment, and large interval spacing as SIBs electrode, the electrochemical performance shall usher in a great enhancement.

Taking antimony (Sb) as an example, it has been widely
65 investigated because it is cheap, abundant, and environmentally friendly.[17] The abundance of Sb in the Earth's crust is estimated at 0.2 to 0.5 parts per million. In addition, Sb has been found in over 100 mineral species. Sb is considered a promising anode material for SIBs due to its large Na storage capacity of 660 mAh g^{-1},
70 good electronic conductivity, and moderate operating voltage.[17] However, the practical application of Sb is mainly hindered by

the massive volume changes (about 390%) during repeated sodiation/desodiation processes. Such volume variation results in severe pulverization and subsequent loss of electrical contact within electrodes, consequently greatly decreasing the cycling life and rate capability of electrodes.[4,18] Indeed, pure Sb powders showed a high initial capacity of 624 mAh g^{-1}, while the capacity abruptly decreased to less than 100 mAh g^{-1} after 25 cycles.[19]

In this work, we firstly report large-scale highly ordered Sb nanorod arrays with uniform large interval spacing as an excellent SIBs anode, fabricated by the nanoimprinted AAO templating technique with the assistance of an electrodeposition process. In such a unique architecture, some critical features are worthwhile to be noted. First, each Sb nanorod possesses uniform nanosized diameter, which could shorten Na ions diffusion pathway. Second, Sb nanorod arrays show the perfect vertical alignment and attendant large interval spacing, which provide direct channels for electrolyte to permeate into the deep portions of arrays, then Na ions can fully contact Sb nanorods without dead angels, improving Na ions accessibility. Meanwhile, the large interval spacing in arrays can also prevent the pulverization by facile strain relaxation during cycling. Third, Sb nanorods themselves as electric conductors directly connecting with the conductive Au/Ni substrate, offering fast and accessible electrons transport, which is very beneficial to the remarkable improvements on the rate capability. Finally, the good adhesion between arrays and conductive substrate can ensure the robust arrays integrity to accommodate volume changes upon cycling.

Within the expectation, in return for its pathbreaking electrode design, the as-prepared Sb nanorod arrays, as additive- and bind-free anodes for SIBs, show a high capacity of 620 mAh g^{-1} at the 100th cycle with a retention of 84% up to 250 cycles, and superior rate capability for delivering reversible capacities of 579.7 and 557.7 mAh g^{-1} at 10 and 20 A g^{-1}, respectively. To our best knowledge, this is the best electrochemical performance in comparison with previously reported Sb-based anodes for SIBs (Table 1). Moreover, a full cell constructed by P2-Na$_{2/3}$Ni$_{1/3}$Mn$_{2/3}$O$_2$ cathode and Sb nanorod arrays anode was also investigated, which delivered a good cycle performance up to 250 cycles, high rate capability even at 20 A g^{-1}, and large energy density up to 130 Wh kg^{-1}. We believe that these excellent electrochemical performances shall arouse high attention to develop more efficient electrode structures for energy storage system.

2. Experimental

2.1 Synthesis of nanoimprinted AAO templates

Nanoimprinted AAO template was prepared using nanoimprinting technique followed by an anodization process. Clean high-purity (99.99%) aluminum foil was electrochemically polished in a 1:7 (v:v) solution of HClO$_4$ and ethanol at a voltage range of 20-30 V. The Ni imprinting stamp was placed on polished Al foil, and the imprinted Al foil was obtained using an oil pressing system under a pressure of about 10 kN cm^{-2} for 3 min. Then the anodization was carried out under a constant voltage of 160 V in 0.4 M H$_3$PO$_4$ at 5°C for 30 min, in which the anodization voltage was chosen to satisfy the distance periods in the imprinting stamp owing to the linear relationship (2.5 nm V^{-1})

between the interpore distance (400 nm) and anodization potential (160 V). After anodization, a 50 nm thick layer of Au were evaporated by physical vapor deposition (PVD), and then a thick layer of Ni was electrochemically deposited on the top of the AAO template with Au as current-carrying substrate, where Au was used to improve the adhesion between Ni layer and template. The backside Al was removed by a mixture solution of CuCl$_2$ (85 wt%) and HCl (15 wt%), and then was transferred to H$_3$PO$_4$ solution (5 wt%) at 30 °C to remove the barrier layer and widen the size of the pores. The time for the barrier layer removal and pore-widening process depends on the desired sizes of pores in the AAO template. At last, a through-pore AAO template with conductive substrate was achieved.

2.2 Synthesis of Sb nanorod arrays

Sb nanorod arrays were electrodeposited inside the above nanoimprinted AAO templates at a constant current density of 1.0 mA cm^{-2} in an electrolytic bath containing SbCl$_3$ and C$_6$H$_5$Na$_3$O$_7$·2H$_2$O. The electrodeposition was conducted in a two-electrode cell with AAO template as the working electrode and Pt foil as counter electrode. Sb nanorod arrays are released by dissolving the AAO template in a NaOH solution (3.0 M) for 30 min, followed by a rinsing process with deionized water. As reference samples, A-Sb NRs, A-2-Sb NRs, and A-2-Sb NRs were also prepared using the similar procedures.

2.3 Synthesis of layered P2-Na$_{2/3}$Ni$_{1/3}$Mn$_{2/3}$O$_2$

The P2-Na$_{2/3}$Ni$_{1/3}$Mn$_{2/3}$O$_2$ was prepared by a co-precipitation method with nickel and manganese nitrates in a stoichiometric amount with sodium hydroxide. Na$_2$CO$_3$ was added afterwards as the sodium source. The calcinations were taken at 600 °C for 4 h and 900 °C for 10 h in air.[20-22]

2.4 Characterization

SEM and TEM measurements were performed on a Hitachi S4800 instrument with voltages of 5 kV and 30 kV, respectively. HRTEM measurement was performed on a Tecnai 20 S-Twin from Philips. XRD measurement was carried out on a Bruker-axs Discover D8 applying Cu Kα (1.54056 Å) radiation equipment. For post-cycling SEM measurement, Sb nanorod arrays electrodes after electrochemical cycling tests were carefully disassembled and washed with PC solution in glove box, and dried at 60°C in a vacuum oven. For HRTEM tests, the samples were scraped from the substrate and dispersed in ethanol followed by ultra-sonication.

### 2.5 Electrochemical Measurements

Electrochemical measurements of half cells were taken using CR2032 coin-type cells with sodium metal as both counter and reference electrode. Sb nanorod arrays were used anodes without any additives of conductive carbon and binder. The mass loading of the active material is around 0.4 mg cm^{-2}. P2-Na$_{2/3}$Ni$_{1/3}$Mn$_{2/3}$O$_2$ was employed as cathode which was prepared by mixing 80% P2-Na$_{2/3}$Ni$_{1/3}$Mn$_{2/3}$O$_2$, 10% acetylene black, and 10% poly(vinylidene fluoride) (PVDF) by weight with an appropriate amount of 1-methyl-2-pyrrolidinone (NMP). The above mixture was pressed onto an aluminum foil which served as a current collector with a subsequent drying process at 120 °C

in vacuum for 12 h. The coin batteries were assembled in a nitrogen-filled glove box with a glass fiber separator (Whatman, GFB/55) and the electrolyte solution of 1.0 M NaClO$_4$ in EC: PC (1:1 by volume) with the addition of 5% fluoroethylene carbonate (FEC). Cyclic voltammetry (CV) was tested on a BioLogic VSP potentiostat. Electrochemical impedance spectroscopy (EIS) was also conducted on a BioLogic VSP potentiostat with frequency of 1 MHz to 10 mHz at the discharge state (0.01 V) after the 1st, 20th, and 50th cycle. The galvanostatic charge-discharge tests were performed at various current densities on LAND-CT2001A test system (Wuhan, China). All of these experiments were conducted at room temperature.

The full cell was assembled using an electrolyte solution of 1.0 M NaClO$_4$ in EC: PC (1:1 by volume) with 5% FEC and galvanostatically cycled with the voltage range of 4.0 to 1.4 V at a current density of 0.5 A g^{-1} (respect to the anode mass). To ensure a suitable positive-to-negative (P/N) capacity ratio for proper cell balance, the P2-Na$_{2/3}$Ni$_{1/3}$Mn$_{2/3}$O$_2$ to Sb nanorod arrays mass loading ratio was about 18.

3. Results and Discussion

The sample preparation procedure is schematically illustrated in Scheme 1. The detailed explanation to prepare nanoimprinted AAO template with the conductive layers of Au and Ni (Step I to IV) can be found in experimental section. Sb nanorod arrays are achieved by electrodepositing Sb precursor inside AAO template (Step V) and subsequently dissoluting the AAO template (Step VI). The electrodeposition represents a cost-effective and mature technique to obtain nanoarrays. The structural parameters of the Sb nanorods can be easily adjusted by changing the experimental parameters of both template fabrication and electrochemical deposition. At last, Sb nanorod arrays were directly used for assembling sodium cells without use of carbon black and binder, which shall largely avoid undesirable interfaces in the electrode material.
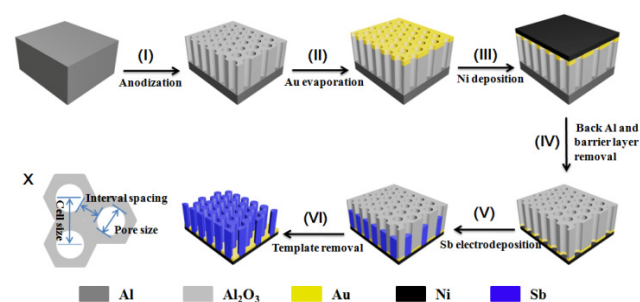
Scheme 1 Schematic illustration of the fabrication processes of Sb nanorod arrays by using the nanoimprinted AAO templating technique with the assistance of an electrodeposition process. X) Size schematic of AAO template.

Fig. 1 shows scanning electron microscopy (SEM) images of the nanoimprinted AAO template (Fig. 1a and b), and Sb nanorod arrays (Fig. 1c-f). As displayed in Fig. 1a and b, the hexagonal arranged pores of AAO template are perfectly uniform in large-area, and the pore size is about 210 nm. It is worth mentioning that both the size and depth of pores can be accurately adjusted to

obtain the desired size depending on the time of pore-widening and anodization, respectively. Fig. 1c-f illustrate the top and tilted views of the as-prepared Sb nanorod arrays which keep the highly ordered and vertically well-aligned growth in large-scale. As is clearly seen from the insets in Fig. 1d and f, Sb nanorods possess the uniform diameter of about 210 nm, and the interval distance among nanorods is as large as 190 nm, as defined by the pore size of as-prepared AAO template. In this work, we used the cell size of nanoimprinted AAO template is 400 nm, and larger cell size (800 nm) also can be obtained, as shown in Fig. S1. By using that (800 nm AAO template), larger interval spacing should be easily controllable.

Fig. 1g reveals an optical image of Sb nanorod arrays directly grown on Au/Ni substrate. It clearly illustrates that Sb nanorod arrays with Au/Ni substrate can be severely rolled without visible signs of degradation, implying the good adhesion and mechanical robustness of the arrays. This feature might indicate our electrodes for a possible application in flexible electronics. As shown in Figure 1g inset, highly ordered Sb nanorod arrays are obtained over a large area (around cm^2-sized range). Larger areas can also be easily achievable by using the larger-sized Ni imprinting stamp combined well-established roll to roll process. The X-ray diffraction (XRD) pattern of the as-prepared Sb nanorod arrays is shown in Fig. S2. Except for the reflections of the substrate (Au and Ni), all the other diffraction peaks can be readily indexed to the rhombohedral Sb phase (JCPDS No. 35-0732) without any impurity, indicating the successful synthesis of Sb. Transmission electron microscopy (TEM) image (Fig. 1h) clearly shows the diameter and length of Sb nanorod are about 210 nm and 1.5 μm, respectively. High resolution TEM (HRTEM) image in Fig. 1i exhibits the lattice fringes with the distance of 3.09 Å, corresponding to the (012) planes of rhombohedral Sb, further confirming the high crystallinity of the sample. The selected area electron diffraction (SEAD) pattern in Fig. 1i inset proves that the Sb nanorods are polycrystalline. Successful growth of such highly ordered and vertically well-aligned Sb nanorod arrays with large interval spacing may offer high ion accessibility, direct electron and ion transport, and robust electrode integrity. Therefore, a promising electrochemical performance is highly expected.

For electrochemical evaluation, Sb nanorod arrays were directly used as anodes for Na coin cells. Fig. 2a shows representative cyclic voltammogram (CV) of the initial ten cycles at a scan rate of 0.5 mV s^{-1} between 0.01 and 2.0 V (vs. Na$^+$/Na). In accordance with previous reports,[23-28] it clearly presents that the first sodiation scan curve is distinctively different with that of the following ones, suggesting an activation process during the first sodiation process. The first sodiation of Na occurs along one sharp current peak at 0.323 V, together with two obscure current peaks at 0.461 and 0.283 V. However, in the second sodiation scan, four distinct current peaks at 0.614, 0.355, 0.309, and 0.130 V are shown. The peak at 0.130 V may be induced by the incomplete sodiation of the former steps in the activation process,[26] then disappears in the subsequent ones. Other three sodiation peaks are continuously shown, whereas shifting to higher potentials and remaining stable in their shapes and intensities in the following ones, suggesting the occurrence of stable sodiation reactions.[29] In the first desodiation scan, there are

one broad peak at 0.835 V and one sharp peak at 0.977 V, which keep showing in the subsequent scans, while slightly shifting to lower potentials. As a consequence, the voltage difference between sodiation and desodiation process is lessening, reflecting smaller polarization.
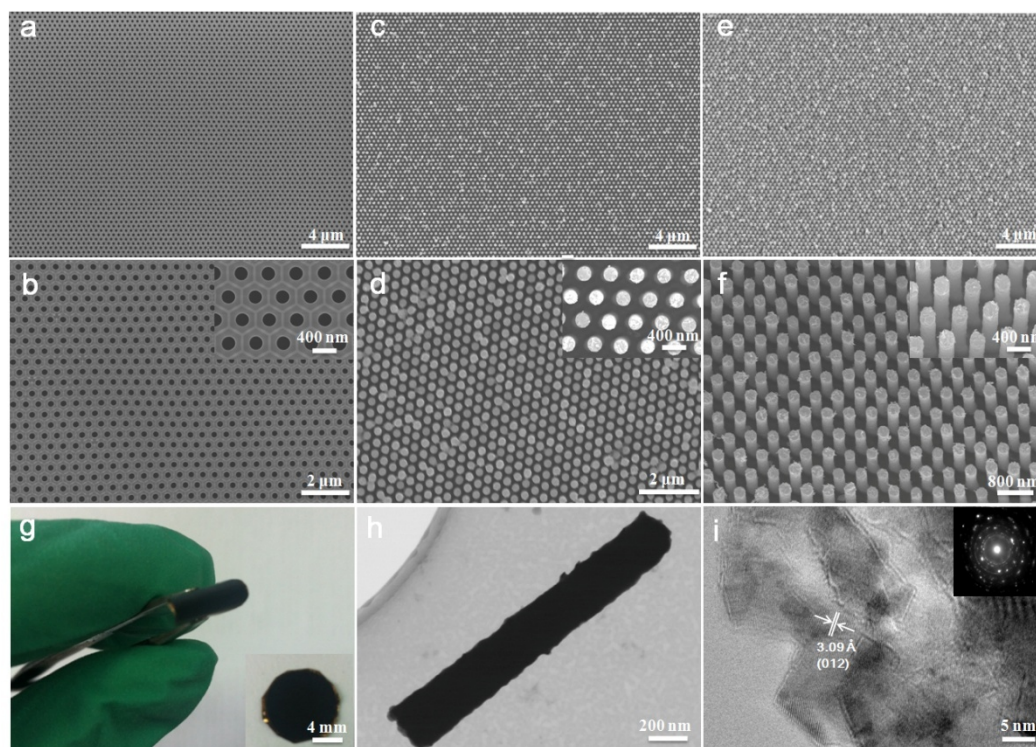

Fig.1 SEM images of nanoimprinted AAO template (a, b), top view (c, d) and tilted view (e, f) of Sb nanorod arrays. g) Optical image of Sb nanorod arrays on Au/Ni substrate. h) TEM image of a single Sb nanorod. i) HRTEM image of Sb nanorods and SAED pattern (inset).

Galvanostatic charge/discharge curves of Sb arrays electrode at a current density of 0.5 A g^{-1} are displayed in Fig. 2b, which show typical characteristics of Sb electrodes.[25-28] In the first discharge curve, it shows the presence of three sodiation plateaus, which are a short slope at 0.590 V, a long plateau at 0.502 V, and a much shorter one at 0.391 V. These three plateaus constantly show in the following curves, corresponding to the sequence of amorphous Sb → amorphous Na$_3$Sb → Na$_3$Sb(hex)/Na$_3$Sb(cub) → Na$_3$Sb(hex).[25-28] In the first charge curve and the subsequent ones, two pronounced disodiation plateaus are constantly shown, which are a long plateau at 0.800 V and another short one at 0.898 V, corresponding to the process of Na$_3$Sb(hex) → amorphous Sb transition and partial crystallization of Sb, respectively.[25-28] All of these voltage profiles are in good agreement with the CV results in Fig. 2a. Furthermore, it is worthwhile to be emphasized that the voltage profiles of both sodiation and desodiation are perfectly reproducible from cycles 1 to 100, indicating the stable structure of Sb nanorod arrays and excellent electrochemical reversibility during cycling.

As shown in Fig. 2c, Sb nanorod arrays anode demonstrated excellent cycling performance. At a current density of 0.2 A g^{-1}, it delivered a high capacity of 620 mAh g^{-1} at the 100th cycle, and 521 mAh g^{-1} at the 250th cycle with a capacity retention of 84%. The cycling performance is comparable to those reported results regarding Sb-based anodes (Table S1). The capacity decay of Sb nanorod arrays was attributed to inevitable increasing thick SEI film and huge volume changes of Sb anode upon cycling, as shown in Fig. S3. The decay can also be accordingly reflected on charge/discharge profiles in different cycles (Fig. S4). It is worthwhile noting that the cycling performance of this anode was obtained without any sophisticated chemical modification of Sb material. It is reported that the protective coating by carbon or other materials can effectively tolerate the massive volume changes and alleviate the stress strain during the Na alloying/dealloying reaction.[19,23,24,30] Therefore, we deduce that such strategy could be the direction of further improvement on cycling performace. The areal capacity of Sb nanorod arrays is also calculated, which is about 215 µAh cm^{-2} at a current density of 80 µA cm^{-2}. The Coulombic Efficiency (CE) for the first cycle is around 78.2%, while it stabilizes at around 97.8% for the following cycles, indicating facile and efficient ions and electrons transport in this electrode.[31-33] When cycled at a large current density of 0.5 A g^{-1}, Sb nanorod arrays showed almost the same capacity with that at 0.2 A g^{-1}, but shorter cycle life due to more serious morphology changes.
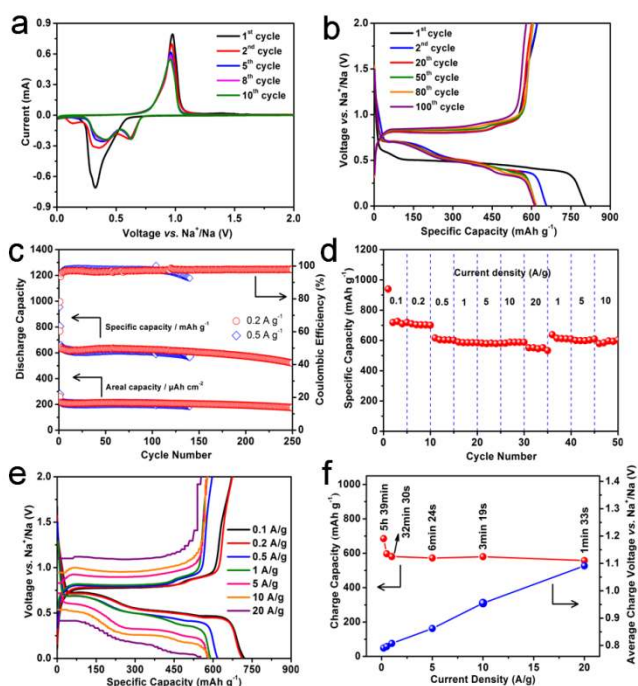
Fig.2 Electrochemical performance of Sb nanorod arrays anode. a) Cyclic voltammetry at a scan rate of 0.5 mV s^{-1} between 0.01 to 2.0 V (*vs.* Na$^+$/Na). b) Galvanostatic charge/discharge voltage profiles in different cycles at a current density of 0.5 A g^{-1}. c) Cycling performance at current densities of 0.2 (80 μA cm^{-2}) and 0.5 A g^{-1} (32 μA cm^{-2}). d) Rate performance and e) corresponding charge/discharge voltage profiles at various current densities from 0.1 to 20 A g^{-1}. f) Respective charge capacity and average charge working potential at various current densities.

In addition to the high capacity and cyclability, Sb nanorod arrays anode also displays remarkably high rate capability. Fig. 2d demonstrates the rate performance investigated at various current densities from 0.1 to 20 A g^{-1}. It is striking to note that Sb nanorod arrays electrode still can be reversibly cycled at super high current densities of 10 and 20 A g^{-1} and deliver large capacities of 579.7 and 557.7 mAh g^{-1}, respectively, indicating the fast transfer of Na ions and electrons through Sb nanorod arrays. When the current densities are reset to 1, 5, and 10 A g^{-1}, the capacities fully recovered and are even slightly higher than those of the first set at the same current densities, implying that the unique electrode structure can preserve the integrity of the electrode and accommodate huge change of current density, which is highly crucial for high power applications of rechargeable batteries. As far as we know, this is the best rate capability in comparison with the previously reported Sb-based anodes in SIBs, as shown in Table 1. The corresponding voltage profiles of the electrode at various current densities are presented in Fig. 2e. As current density increasing from 0.1 to 20 A g^{-1}, the charge/discharge voltage profiles have similar shapes, with minimal increase of the voltage offset, even at ultra-high current

density of 20 A g^{-1}, suggesting facile electron transport and small mechanical energy loss of the electrode. Moreover, when the current density is reduced back to 1 A g^{-1} (Fig. S5), the voltage profiles recovered and are perfectly reproducible in comparison with that of the first set at the same current density (1 A g^{-1}), reflecting the stable structure of Sb nanorod arrays to strongly tolerate the repeated and rapid Na alloying/dealloying reactions. Charge working potentials of the electrode at different current densities are shown in Fig. 2f. The potentials only display a small increase of 0.027 V when the current is raised from 0.1 to 1 A g^{-1}, and an increase of 200 times of the current brings an increase of the potential of only 0.311 V when the current is raised to 20 A g^{-1}, indicating the excellent structure stability of Sb nanorod arrays and fast electron transport. In addition, the charging time are 6 min 24 s, 3 min 19 s, and 1 min 33 s at the current densities of 5, 10, and 20 A g^{-1}, with high charge capacities of 572.4, 579.7, and 557.7 mAh g^{-1}, respectively. The electrodes can be charged and discharged at such high rates with such high capacities in such short time, which are highly desired for high power and energy devices.

As clearly illustrated in the above results, highly ordered Sb nanorod arrays anode shows extremely large capacities, excellent cycle stability, and superior rate capability for Na-ion storage, which can be ascribed to its pathbreaking electrode design on the basis of the following factors. First, the nanoscaled diameter of Sb nanorods can shorten Na ion diffusion pathway compared to the bulk Sb powders. Nanostructuring of the active materials can also moderate the effect of volume changes and enhance kinetics of the conversion and alloying reactions.[38-40] Second, Sb nanorod arrays themselves as electric conductors directly connect to the conductive Au/Ni substrate offering fast and accessible electron transport, giving rise to superior rate capability. Third, Sb nanorod arrays show well vertical alignment and uniform large interval spacing (about 190 nm), which provide direct channels for electrolyte and ions to permeate into all the portions of arrays, and thus Na ions can fully contact Sb nanorods without any dead angels, improving Na ion accessibility. This point surpasses the traditional materials including powder-based materials and disordered network that charge carriers must move through the interstitial regions or spaces within materials to access the internal part. Owing to this feature as well as the large surface area of Sb nanorod arrays, large capacities at high rates are obtained. Moreover, the large interval spacing in arrays can prevent the pulverization by facile strain relaxation during cycling. The third point is extremely significant to ensure Sb nanorod arrays to show high capacities, long-term cycling stability, and excellent rate capability. In order to better reveal the advantages of highly ordered arrays with large interval spacing, we conducted parallel comparative tests between vertically well-aligned Sb nanorod arrays (S-Sb NRs) and attached Sb nanorod arrays (A-Sb NRs) with very limited interval spacing for the permeation of electrolyte (relating to Na ion transport and strain release) on the electrochemical performance. These two arrays have the same length of 1.5 μm, and more detailed structure parameters of A-Sb NRs can be found in Table S2.

Table 1. Electrochemical performance comparison of the as-prepared Sb nanorod arrays with previously reported Sb-based anodes.

Materials	Current density, A g^{-1}	Cycling Capacity, mAh g^{-1} 2nd	50th	100th	Rate Capability, mAh g^{-1} (current density, A g^{-1})	
Nanocomposite Sb/C[19]	0.1	610	570	575	489 (1)	309 (2)
SnSb/C nanocomposite[23]	0.1	~540	435	/	433 (0.2)	274 (1)
Sb/C fibers[24]	0.1	~425	~420	400	300 (1)	104 (6)
Monodisperse Sb Nanocrystals[25]	0.66	~590	~560	~580	~550 (5.28)	~520 (13.2)
Bulk Sb[26]	0.33	~540	~560	~570	506 (1.32)	491 (2.64)
Sb/MWCNT nanocomposite[27]	0.2	~510	~450	~400	350 (1)	225 (2)
Sb porous hollow microspheres[28]	0.66	574.9	~520	502.3	470.3 (1.6)	312.9 (3.2)
SnSb-porous carbon nanofibers[29]	0.1	349	350	350	198 (5)	113 (10)
Sb-C nanofibers[34]	0.2	~495	~500	~490	382 (1.8)	337 (3)
Porous Sb/Cu$_2$Sb anode[35]	0.066	~660	~550	~480	~470 (0.66)	~170 (3.3)
Rod-like Sb-C composite[36]	0.05	~650	~440	~431	~500 (0.05)	~259 (0.25)
Sn-Ge-Sb alloys[37]	0.085	833	662	/	~420 (4.25)	381 (8.5)
Sb nanorod arrays (this work)	0.5	655.7	618.4	612.6	579.7 (10)	557.7 (20)

Fig. 3 demonstrates the different Na ion transport modes in these two arrays, noting that metal Sb is a good electric conductor and it can effectively transfer electrons between conductive substrate and nanorods without the help of conductive additive carbon. As shown in Fig. 3a and b, due to the large interval spacing in vertical well-aligned arrays, Na ions can easily diffuse into the matrix in S-Sb NRs, resulting to superior Na ion accessibility, thus large capacities are highly expected, especially at high current densities. In contrast, SEM image (Fig. 3c) of A-Sb NRs displays severe agglomerated nanorods and attendant very limited interval spacing in arrays. Therefore, the electrolyte is very difficult to directly penetrate into the bottom region of A-Sb NRs through the top of attached nanorods (Fig. 3d). As a substitute, Na ions have to diffuse through interstitial regions within arrays, which would lead to incomplete active sites for Na$^+$, then showing decreased capacities of A-Sb NRs. On the other hand, the large interval spacing in S-Sb NRs can provide a facile strain relaxation during cycling, thereby preventing the pulverization. However, for A-Sb NRs, the joint parts tend to break since the stress existed among these entangled Sb nanorods, leading to poor transport of electrons and ions, thereby rapid capacity decay.[41,42]

Based on the above analysis of different Na ion transport and strain release modes, we investigated the electrochemical performance of A-Sb NRs and S-Sb NRs under the same testing conditions. As shown in Fig. 4a, the A-Sb NRs have the similar CV curves with S-Sb NRs (Fig. 2a), indicating the identical sodiation/desodiation mechanism. However, the capacities and cycling stability are far less than those of S-Sb NRs. In Fig. 4b, A-Sb NRs show a first discharge capacity of 529.5 mAh g^{-1} and CE of 79.5% at a current density of 1 A g^{-1}. In the following 50 cycles, A-Sb NRs keep stable discharge capacity of around 475 mAh g^{-1}, however, the CE gradually decreases, implying the irreversible reactions occurred during this period. From the 50th cycle, A-Sb NRs undergo rapid capacity decay, delivering only 345.1 mAh g^{-1} in the 60th cycle. The galvanostatic charge/discharge voltage profiles of A-Sb NRs (Fig. S6) further

reveal this decay phenomenon from another point of view. In the 50th cycle, the discharge plateau appears a big decrease from 0.37 V in 10th cycle to 0.17 V and the flat charge plateau at 0.87 is replaced by a big slope. In contrast, an excellent cycling stability of S-Sb NRs is observed at the same current density and the electrode still can retain a constant and even slightly ahead of capacity of 625.2 mAh g^{-1} over 60 cycles and high CE of around 98% (except the first cycle of 83%) (Fig. 4c). Furthermore, the voltage profiles of S-Sb NRs (Fig. S7) present perfect reproducibility during 50 cycles. Notably, it is as expected that the capacity, CE, and cycling stability of S-Sb NRs are much better than those of A-Sb NRs, which is largely ascribed to more efficient ion transport, as well as more facile strain release in S-Sb NRs.
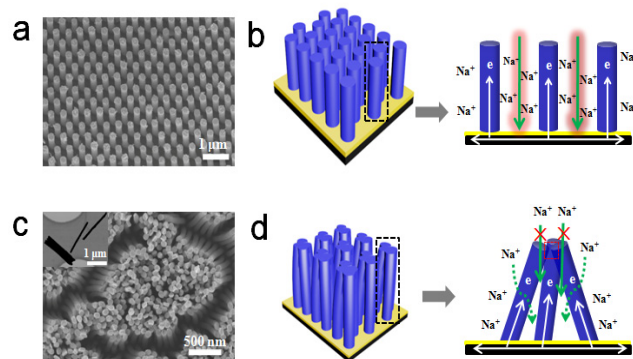
Fig. 3 SEM images of a) S-Sb NRs and c) A-Sb NRs (Inset: TEM image of A-Sb NRs). Corresponding schematic illustration of transport mechanism of Na ions and electrons in b) S-Sb NRs and d) A-Sb NRs.

Nyquist plots of A-Sb NRs and S-Sb NRs are displayed in Fig. 4d and e to investigate their resistance change with the increased cycles. From the first cycle to 50th cycle, A-Sb NRs show a gradually increased resistance (Fig. 4d). However, for S-Sb NRs,

the change of resistance is negligible (Fig. 4e), further confirming relatively easier Na ion transport in S-Sb NRs, thereby reducing the irreversible capacity loss and enhancing cycling performance. For the rate performance of A-Sb NRs electrode (Fig. 4f), it demonstrates the similar trend with S-Sb NRs in the first 45 cycles but with lower capacities. In addition, from the 46th cycle (a current density of 10 A g^{-1} in the second rate set), the capacities rapidly decrease. Under high current densities, the electrode needs to finish the charge and discharge processes in a very short time. Therefore, high ions accessibility, good electrical conductivity, and stable electrode structure are essential. A-Sb NRs electrode shows limited ions accessibility, and the attached structure of is not conducive to release strain induced by volume expansion, resulting in unstable electrode structure. As a sum result, under the high current density of 10 A g^{-1} in the second rate set, A-Sb NRs electrode displays rapid capacity decay. The largely different electrochemical performance between A-Sb NRs and S-Sb NRs fully supports our assumption of the predominance of this highly ordered alignment with large interval spacing electrode design for Na-ion storage. To more comprehensively reveal the importance of highly ordered arrays with interval spacing, we also compared the electrochemical performance of another two kinds of arrays, as shown in Table S2 and Fig. S8.
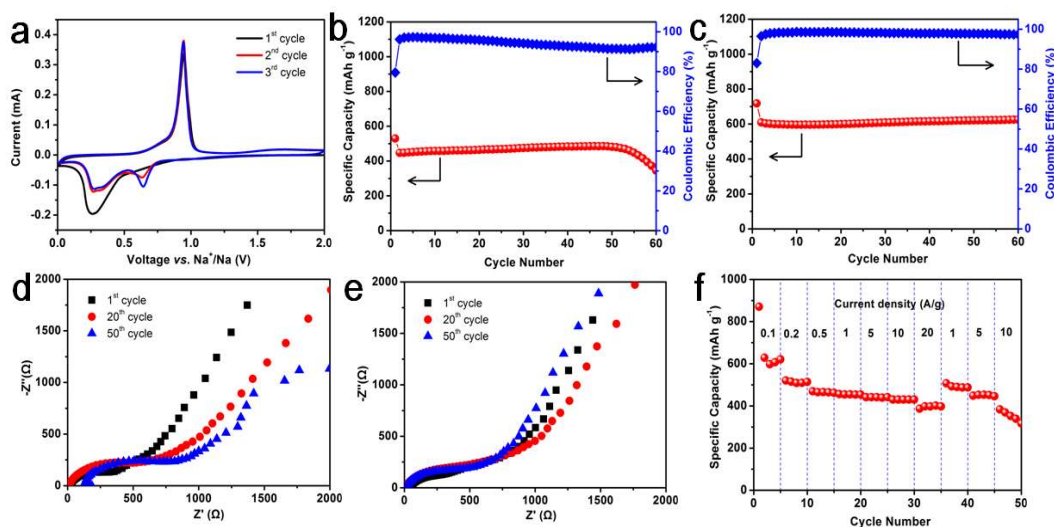

Fig. 4 a) Cyclic voltammetry of A-Sb NRs electrode at a scan rate of 0.5 mV s^{-1} between 0.01 to 2.0 V (*vs.* Na^+/Na). Cycling performance of b) A-Sb NRs and c) S-Sb NRs at a current density of 1 A g^{-1}. Nyquist plots of d) A-Sb NRs and e) S-Sb NRs at discharge state (0.01 V) from 1 MHz to 10 mHz. f) Rate performance of A-Sb NRs electrode at various current densities from 0.1 to 20 A g^{-1}.

In addition, the remarkable electrode integrity is also largely beneficial for the excellent electrochemical performance. The good adhesion between Sb nanorod arrays and conductive substrate can ensure the robust arrays integrity to accommodate volume expansion/contraction upon cycling, resulting in good cycling and rate performance. To better verify this point, the morphology of Sb nanorod arrays after long-term cycling was also investigated. Fig. 5 shows SEM and TEM images of Sb nanorod arrays cycled at a current density of 10 A g^{-1} after 70 cycles in fully desodiation state. As can be seen from the top (Fig. 5a) and side view (Fig. 5b), Sb nanorod arrays still maintain their highly ordered and vertically well-aligned feature with clear interval spacing after long-term cycling at such high current density, which prevents pulverization and preserves electrode integrity, giving rise to excellent cycling and rate performance. We scratched Sb nanorods off the substrate and observed the uniform and well-preserved Sb nanorods on TEM (Fig. 5b inset) image. The diameter and length of the cycled Sb nanorod are around 300 nm and 2.1 μm, respectively, and larger than those of the pristine Sb nanorod (Fig. 1h) with rough surfaces, deriving from the volume expansion/contraction in repeated sodiation/desodiation processes. Despite the volume change, there is no structural collapse and agglomeration of Sb nanorod arrays, suggesting the chemical and mechanical robustness of the arrays electrode. Based on the above four major advantages of the electrode structure, Sb nanorod arrays anode showed the overall excellent electrochemical performance for Na-ion storage.
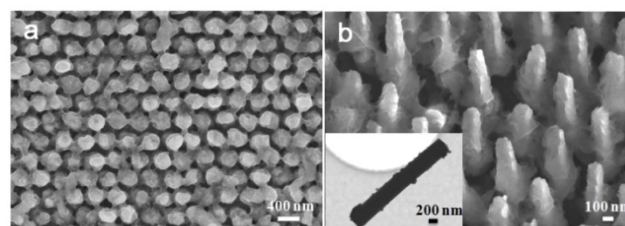

Fig. 5 SEM images of a) top view and b) tilted view of Sb nanorod arrays electrode after 70 cycles at a current density of 10 A g^{-1}. (Inset: TEM image of a single Sb nanorod.)

To display the feasibility of Sb nanorod arrays in full-cell configuration, a full cell coupled by P2-$Na_{2/3}Ni_{1/3}Mn_{2/3}O_2$ cathode and Sb nanorod arrays anode was investigated. The structure and electrochemical performance characterizations of P2-$Na_{2/3}Ni_{1/3}Mn_{2/3}O_2$ can be seen in Fig. S9 and Fig. S10. This full cell was tested with a voltage range of 1.4-4.0 V at a large current density of 0.5 A g^{-1} (with respect to the anode weight) using 1.0 M $NaClO_4$ in EC-PC-5% FEC electrolyte. According to the

average working potentials of 3.6 and 0.7 V *vs.* Na$^+$/Na for P2-Na$_{2/3}$Ni$_{1/3}$Mn$_{2/3}$O$_2$ cathode (Fig. S10b) and Sb nanorod arrays anode (Fig. 2b), respectively, it is reasonably deduced that the full cell operates at around 2.9 V, as indeed shown by Fig. R6a reflecting charge/discharge profiles of the full cell. Fig. R6b shows the cycling performance of this full cell, in which it delivered a superior capacity retention of around 94% before 110 cycles with a capacity of around 620 mAh g^{-1} (relative to Sb anode weight), which is very close to the theoretical capacity of Sb (660 mAh g^{-1}). From the 110th cycle to the 130th cycle, this cell showed a capacity decay to 450 mAh g^{-1}. This decay characteristic is similar with Na/Sb half cell, due to the inevitable morphology change of Sb (Fig. S3). Nevertheless, at such a high current density of 0.5 A g^{-1}, this cell still can work with a high capacity of about 334 mAh g^{-1} up to 250 cycles and extremely stable CE of around 98%. Although the capacity of the 250th cycle is only 54% the 110th capacity, the value of 334 mAh g^{-1} is very attractive considering at such large current density of 0.5 A g^{-1}. Moreover, according to the above studies, the cycling stability of this full cell might be better at a lower current density.
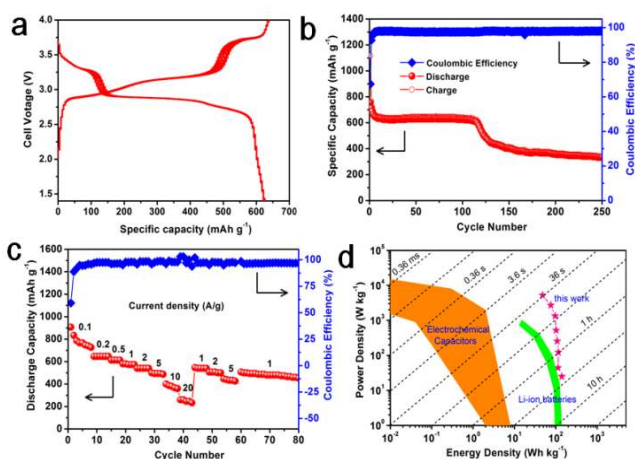

Fig. 6 Electrochemical performance of a full cell coupled by P2-Na$_{2/3}$Ni$_{1/3}$Mn$_{2/3}$O$_2$ cathode and Sb nanorod arrays anode. a) Galvanostatic charge/discharge voltage profiles of five cycles, and b) Cycling performance at a current density of 0.5 A g^{-1} (relative to the anode weight). c) Rate Capability (with respect to the anode weight), and d) Ragone plot of energy and power density (with respect to the total mass of anode and cathode) at various current densities from 0.1 to 20 A g^{-1}. The shaded curves were obtained from ref. 42.

Notably, this full cell also displayed high rate capability, as shown in Fig. R6c. Benefiting from the great rate capability of the Na/Sb half cell, it can be cycled at very large current densities of 10 and 20 A g^{-1}, and maintained stable reversibility. In addition, these capacities can be fully recovered when the cell went back to the low current densities. The energy density and power density of the full cell were further evaluated with a Ragone plot, which were calculated based on the total mass of the cathode and anode active materials, as shown in Fig. R6d. These values show a clear comparison with commercial lithim-ion batteries and electrochemical capacitors. Such cell could provide much higher power densities than commercial Li-ion batteries,

while the energy densities are several times bigger than that of electrochemical capacitors. These capabilities suggest that Sb nanorod arrays anodes can be used to build large energy storage and conversion devices with both high-power and high-energy densities.

4. Conclusions

In summary, we presented a large-scale highly ordered Sb nanorod arrays with uniform large interval spacing. Used as SIBs anode, Sb nanorod arrays delivered a high capacity retention of 84% up to 250 cycles. Remarkably, the anode showed superior rate capability with high capacities of 579.7 and 557.7 mAh g^{-1} at 10 and 20 A g^{-1}, respectively, and fully recovered the low rate capacities. The excellent electrochemical performance is achieved in return for its pathbreaking electrode design which ensures high Na ion accessibility, fast electron transport, and strong structural integrity. Moreover, the successful application of such full cell indicates that Sb nanorod arrays anodes can be used to build large energy storage and conversion devices with both high-power and high-energy densities.

Acknowledgments

Notes and references

Institute for Physics and IMN MacroNano®, Technical University of Ilmenau, Ilmenau 98693, Germany. Fax: +49(0)3677 69-3746; Tel: +49(0)3677 69-3748; E-mail: yong.lei@tu-ilmenau.de

1. V. Palomares, P. Serras, I. Villaluenga, K. B. Hueso, J. Carretero-Gonzalez and T. Rojo, *Energy Environ. Sci.*, 2012, **5**, 5884-5901.
2. S. W. Kim, D. H. Seo, X. H. Ma, G. Ceder and K. Kang, *Adv. Energy Mater.*, 2012, **2**, 710-721.
3. S. Y. Hong, Y. Kim, Y. Park, A. Choi, N. S. Choi and K. T. Lee, *Energy Environ. Sci.*, 2013, **6**, 2067-2081.
4. M. D. Slater, D. Kim, E. Lee and C. S. Johnson, *Adv. Funct. Mater.*, 2013, **23**, 947-958.
5. G. Che, B. B. Lakshmi, E. R. Fisher and C. R. Martin, *Nature,* 1998, **393**, 346-349.
6. Y. Li, B. Tan and Y. Wu, *Nano Lett.*, 2008, **8**, 265-270.
7. P. L. Taberna, S. Mitra, P. Poizot, P. Simon and J. M. Tarascon, *Nat. Mater.*, 2006, **5**, 567-573.
8. Z. L. Wang and J. H. Song, *Science*, 2006, **312**, 242-246.
9. A. L. M. Reddy, M. M. Shaijumon, S. R. Gowda and P. M. Ajayan, *Nano Lett.*, 2009, **9**, 1002-1006.
10. J. Jiang, Y. Li, J. Liu and X. Huang, Nanoscale 2011, **3**, 45-48.
11. Y. Liu, Y. Xu, Y. Zhu, J. N. Culver, C. A. Lundgren, K. Xu and C. Wang, *ACS Nano.*, 2013, **7**, 3627-3634.
12. J. Liu Y. Li, X. Huang, R. Ding, Y. Hu, J. Jiang and L. Liao, *J. Mater. Chem.*, 2009, **19**, 1859–1864.
13. L. Wen, Y. Mi, C. Wang, Y. Fang, F. Grote, H. Zhao, M. Zhou and Y. Lei, *Small*, 2014, **10**, 3162-3168.
14. H. Zhao, C. Wang, R. Vellacheri, M. Zhou, Y. Xu, Q. Fu, M. Wu, F. Grote and Y. Lei, *Adv. Mater.*, 2014, **26**, 7654-7659.
15. Z. Zhan AND Y. Lei, *ACS Nano*, 2014, **8**, 3862-3868.

16. Y. Xu, M. Zhou, L. Wen, C. Wang, H. Zhao, Y. Mi, L. Liang, Q. Fu, M. Wu and Y. Lei, *Chem. Mater.*, 2015, **27**, 4274-4280.

17. G. Jeong, Y.-U. Kim, H. Kim, Y.-J. Kim and H.-J. Sohn, *Energy Environ. Sci.*, 2011, **4**, 1986-2002.

18. V. L. Chevrier and G. Ceder, *J. Electrochem. Soc.*, 2011, **158**, A1011-A1014.

19. J. Qian, Y. Chen, L. Wu, Y. Cao, X. Ai and H. Yang, *Chem. Commun.*, 2012, **48**, 7070-7072.

20. Y. Wen, B. Wang, G. Zeng, K. Nogita, D. Yeand L. Wang, *Chem. Asian. J.*, 2015, **10**, 661-666.

21. D. H. Lee, J. Xuand Y. S. Meng, *Phys. Chem. Chem. Phys.*, 2013, **15**, 3304-3312.

22. Z. Lu and J. R. Dahn, *J. Electrochem. Soc.*, 2001, **148**, A1225-A1229.

23. L. Xiao, Y. Cao, J. Xiao, W. Wang, L. Kovarik, Z. Nie and J. Liu, *Chem. Commun.*, 2012, **48**, 3321-3323.

24. Y. Zhu, X. Han, Y. Xu, Y. Liu, S. Zheng, K. Xu, L. Hu and C. Wang, *ACS Nano*, 2013, **7**, 6378-6386.

25. M. He, K. Kravchyk, M. Walter and M. V. Kovalenko, *Nano Lett.*, 2014, **14**, 1255-1262.

26. A. Darwiche, C. Marino, M. T. Sougrati, B. Fraisse, L. Stievano and L. Monconduit, *J. Am. Chem. Soc.*, 2012, **134**, 20805-20811.

27. X. Zhou, Z. Dai, J. Bao and Y. G. Guo, *J. Mater. Chem. A*, 2013, **1**, 13727-13731.

28. H. Hou, M. Jing, Y. Yang, Y. Zhang, Y. Zhu, W. Song, X. Yang and X. Ji, *J. Mater. Chem. A*, 2015, **3**, 2971-2977.

29. L. Ji, M. Gu, Y. Shao, X. Li, M. H. Engelhard, B. W. Arey, W. Wang, Z. Nie, J. Xiao, C. Wang, J. G. Zhang and J. Liu, *Adv. Mater.*, 2014, **26**, 2901-2908.

30. X. Han, Y. Liu, Z. Jia, Y.-C. Chen, J. Wan, N. Weadock, K. J. Gaskell, T. Li and L. Hu, *Nano Lett.*, 2014, **14**, 139-147.

31. B. Luo, B. Wang, X. L. Li, Y. Y. Jia, M. H. Liang and L. J. Zhi, *Adv. Mater.*, 2012, **24**, 3538-3543.

32. C. He, S. Wu, N. Zhao, C. Shi, E. Liu and J. Li, *ACS Nano*, 2013, **7**, 4459-4469.

33. X. L. Jia, Z. Chen, X. Cui, Y. T. Peng, X. L. Wang, G. Wang, F. Wei and Y. F. Lu, *ACS Nano*, 2012, **6**, 9911-9919.

34. L. Wu, X. Hu, J. Qian, F. Pei, F. Wu, R. Mao, X. Ai, H. Yang and Y. Cao, *Energy Environ. Sci.*, 2013, **7**, 323-328.

35. D. H. Nam, K. S. Hong, S. J. Lim and H. S. Kwon, *J. Power Sources*, 2014, **247**, 423-427.

36. L. Fan, J. Zhang, J. Cui, Y. Zhu, J. Liang, L. Wang and Y. Qian, *J. Mater. Chem. A*, 2013, **3**, 3276-3280.

37. B. Farbod, K. Cui, W. P. Kalisvaart, M. Kupsta, B. Zahiri, A. Kohandehghan, E. M. Lotfabad, Z. Li, E. J.; Luber and D. Mitlin, *ACS Nano*, 2014, **8**, 4415-4429.

38. A. Magasinski, P. Dixon, B. Hertzberg, A. Kvit, J. Ayala and G. Yushin, *Nat. Mater.*, 2010, **9**, 353-358.

39. I. Kovalenko, B. Zdyrko, A. Magasinski, B. Hertzberg, Z. Milicev, R. Burtovyy, I. Luzinov and G. Yushin, *Science*, 2011, **333**, 75-79.

40. J. M. Mosby and A. L. Prieto, *J. Am. Chem. Soc.*, 2008, **130**, 10656-10661.

41. C.-H. Lai, K.-W. Huang, J. H. Cheng, C.-Y. Lee, B.-J. Hwang and L. J. Chen, *J. Mater. Chem.*, 2010, **20**, 6638-6645.

42. J. Huang, K. Wang and Z. Wei, *J. Mater. Chem.*, 2011, **20**, 1117-1121.

43. P. Simon and Y. Gogotsi, *Nat. Mater.*, 2008, **7**, 845-854.